Duel Solutions in Hiemenz Flow of an Electro-Conductive Viscous Nanofluid Containing Elliptic Single-/Multi-Wall Carbon Nanotubes With Magnetic Induction Effects

M. Ferdows[1]
Research Group of Fluid Flow Modeling and Simulation;
Department of Applied Mathematics,
University of Dhaka,
Dhaka 1000, Bangladesh
e-mail: ferdows@du.ac.bd

Tahia Tazin
Department of Mathematics,
Comilla University,
Cumilla 3506, Bangladesh
e-mail: tahia@cou.ac.bd

O. Anwar Bég
Multi-Physical Engineering Sciences Group;
Department of Mechanical Engineering;
School of Science, Engineering and Environment (SEE),
University of Salford,
Manchester, UK
e-mail: O.A.Beg@salford.ac.uk

Tasveer A. Bég
Engineering Mechanics Research,
Israfil House,
Dickenson Road,
Manchester M13, UK
e-mail: tasveerabeg@gmail.com

Modern magnetic nanomaterials are increasingly embracing new technologies including smart coatings, intelligent lubricants, and functional working fluids in energy systems. Motivated by studying the manufacturing magnetofluid dynamics of electroconductive viscous nanofluids, in this work, we analyzed the magnetohydrodynamics (MHD) convection flow and heat transfer of an incompressible viscous nanofluid containing carbon nanotubes (CNTs) past a stretching sheet. Magnetic induction effects are included. Similarity solutions are derived where possible in addition to dual branch solutions. Both single-wall carbon nanotubes (SWCNTs) and multi-wall carbon nanotubes (MWCNTs) are considered taking water and kerosene oil as base fluids. The governing continuity, momentum, magnetic induction, and heat conservation partial differential equations are converted to coupled, nonlinear systems of ordinary differential equations via similarity transformations. The emerging control parameters are shown to be Prandtl number (Pr), nanoparticle volume fraction parameter (φ), inverse magnetic Prandtl number (λ), magnetic body force parameter (β) and stretching rate parameter (A), and the type of carbon nanotube. Numerical solutions to the ordinary differential boundary value problem are conducted with the efficient bvp4c solver in MATLAB. Validation with earlier studies is included. Computations of reduced skin friction and reduced wall heat transfer rate (Nusselt number) are also comprised in order to identify the critical parameter values for the existence of dual solutions (upper and lower branch) for velocity, temperature, and induced magnetic field functions. Dual solutions are shown to exist for some cases studied. The simulations indicate that when the stretching rate ratio parameter is less than 1, SWCNT nanofluids exhibit higher velocity than MWCNT nanofluids with increasing magnetic parameters for water- and kerosene-oil-based CNT nanofluids. Generally, SWCNT nanofluids achieve enhanced heat transfer performance compared to MWCNT nanofluids. Water-based CNT nanofluids also attain greater flow acceleration compared with kerosene-oil-based CNT nanofluids. [DOI: 10.1115/1.4055278]

1 Introduction

Stagnation (Hiemenz) flows feature in numerous applications in engineering sciences including, laser materials processing [1], coating dynamics [2], and vapor deposition [3]. Such flows are characterized by the fluid impinging on either a plane (orthogonal) [4] or oblique (non-orthogonal) surface [5] and a symmetric or asymmetric distribution in flow in the vicinity of the stagnation point which can be modeled as a flow toward an infinite flat plate. In thermal materials processing operations [6], liquids are frequently stretched or contracted along the impingement surface. This is achieved by stretching the surface or shrinking it, and this may be done at linear, quadratic, exponential [7,8], or other rates. In simulating such flows, the boundary-layer theory provides a solid framework. Sakiadis [9] initiated the study of viscous flows from a continuously moving solid surface. Crane [10] extended the Sakiadis model to linear stretching sheets. Many subsequent studies have been communicated including heat transfer and representative works include those of Dandapat et al. [11] (on surface tension effects), Tsai et al. [12] (on non-uniform heat generation effects) and Bhattacharyya et al. [13] (on hydrodynamic wall slip in stagnation flow).

A key focus in thermal engineering and materials manufacturing in recent years has been the desire to improve in thermal conductivity of heat transfer fluids. *Nanotechnology* has been a significant aspect of this focus. Among the many nanomaterials developed, "nanofluids" have become increasingly popular owing to their demonstrated versatility in multiple technologies ranging from energy and medicine to environment and transportation [14–17]. Introduced by Choi et al. [18], heat transfer rates have been shown to be significantly elevated via doping conventional base fluids (water, oils, etc.) with a variety of nanoparticles (metallic, carbon-

---

based, etc.). Further experimental corroboration of this behavior has been confirmed by many researchers [19–22]). These studies have shown that even with a small solid volume fraction of nanoparticles (usually less than 5%), the thermal conductivity of nanofluids can be enhanced by 10–50%. Extensive discussion of these trends is documented in the studies by Trisaksri and Wongwives [23], Wang and Majumdar [24], Eastman et al. [25], among others. Mehmood et al. [26] investigated the oblique stagnation flow of nanofluids containing metallic nanoparticles with radiative flux and wall slip effects. Carbon nanotubes (CNTs) are an alternative nanofluid suspension, which have special thermal properties with very high thermal conductivities for their cylindrical carbon molecular origin. Several experimental and theoretical studies of CNT nanofluid dynamics have been reported in recent years. Ding et al. [27] investigated the heat transfer behavior of CNT nanofluids flowing through a horizontal tube, observing that convective heat transfer is enhanced and dependent on the Reynolds number and solid volume fraction of CNTs. Volder et al. [28] presented a detailed appraisal of the commercial and industrial usage of carbon nanotubes. Akbar et al. [29] considered the stagnation point flow of CNT nanofluid from a stretching sheet, highlighting that due to the high density and thermal conductivity of single-wall carbon nanotubes (SWCNTs), the Nusselt number is higher relative to multi-wall carbon nanotubes (MWCNTs). Akbar et al. [30] have also described a second law analysis of CNT nanofluid metachronal pumping and convection.

Magnetohydrodynamics (MHD) [31] involves the interaction of viscous, electrically conducting fluids via the application of external magnetic fields which may be static or oscillating. As such MHD can be utilized very effectively in controlling heat, momentum, and mass transfer in materials processing and can enable significant modifications of material constitution and subsequent performance. Magnetized nanofluid flows have therefore received considerable attention in recent years. Some examples of such works include those of Bég et al. [32] (on transient mixed magneto-convective nanofluid exponentially stretching sheet flow in porous media), Seth and Mandal [33] (on stagnation flow of electromagnetic nanofluids in coating systems), and Thumma et al. [34] (on magnetic nanomaterial thermal stretching on a tilted substrate). However, these studies did not consider CNT-based nanofluids. In recent years, significant progress has been made in modifying CNTs to achieve electromagnetic properties. Magnetic CNT nanofluids can be synthesized via the chemical combination of magnetic nanoparticles or nanocrystals and CNTs in order to obtain nanohybrid structures, through encapsulation of magnetic molecules inside the carbon nanotubes (endohedral functionalization) or grafting/decorating CNTs on their surface (exohedral functionalization) by bioconjugation chemistry or electrochemical deposition. It has been found [35,36] that the thermal conductivity (TC) heat transfer nanofluids can be fabricated which feature both CNTs and magnetic-field-sensitive nanoparticles (e.g., Fe_2O_3). In such functional systems, the Fe_2O_3 particles generate aligned chains under an external magnetic field which assist in connecting nanotubes and effectively boost the thermal conductivity. This behavior is however very sensitive to the duration of magnetic field application since excessive exposure may result in agglomeration of the ferrite nanoparticles and clustering of CNTs which then reduces the thermal conductivity of the nanofluid. A promising additional method of achieving magnetic CNT nanofluids includes manipulation of the chemical structure of, for example, $Mn_{12}Ac$ single-molecule magnets (SMM) and encapsulation within the carbon nanotube. Many further excellent studies of magnetic CNT nanofluids are available in Refs. [37–43]. A further important phenomenon in MHD nanofluid flows is electromagnetic induction. This requires the inclusion of a further balance equation for induced magnetic field and generates more complex effects compared with conventional MHD flows in which a Lorentzian magnetic drag alone is present. Although extensive work has been communicated in conventional viscous MHD flows with induction effects [44–46], relatively sparse attention has been directed at *magnetic induction*

nanofluid transport phenomena. Metallic aqueous nanofluid flows from stretching sheets have been analyzed by Bég et al. [47,48] for a variety of nanoparticles including copper, titanium oxide, silver, and aluminum oxide. Uddin et al. [49] have considered slip stagnation point flow of a magnetic nanofluid over a stretching/shrinking wedge with micro-organism doping. More recently, CNT-based magnetic nanofluids have been scrutinized in the scientific literature. Iqbal et al. [50] used numerical quadrature to compute the CNT nanofluid stagnation point flow with the induced magnetic field, considering both single (SWCNT) and multi-walled (MWCNT) configurations and water- and kerosene-oil-base fluids. They showed that induced magnetic field is an increasing function of solid nanoparticles volumetric fraction and that MWCNTs achieve a more prominent enhancement in the induced magnetic field compared with SWCNTs for both water- and kerosene-oil-based fluids.

Motivated by expanding the understanding of magnetized CNT nanofluid materials processing fluid dynamics with electromagnetic induction included, in the present study, a rigorous examination of plane stagnation flow of such fluids from a stretching surface is described for both SWCNT and MWCNT suspensions. Both water- and kerosene base fluids are considered, and more attention is devoted to the modifications in magnetic induction, temperature, and momentum distributions than previously reported. Computational solutions are presented using the efficient bvp4c solver in MATLAB. Validation with earlier studies is included. Computations of reduced skin friction and reduced wall heat transfer rate (Nusselt number) are also presented in order to establish the critical parameter values for the possible existence of dual solutions, which is another novelty of the current work. A detailed parametric study of the influence of all nanoscale and thermophysical on non-dimension velocity, induced magnetic field, and temperature profiles is conducted. Extensive validation with simpler models in the literature is also included.

2 Magnetic Carbon Nanotube Nanofluid Stagnation Flow Model

The steady two-dimensional stagnation point flow of an electrically conducting incompressible viscous CNT nanofluid toward a linear stretching sheet is considered in a Cartesian coordinate system $(\bar{x}, \bar{y})$. The sheet surface is parallel to the $\bar{x} -$ axis and the nanofluid occupies the region $\bar{y} > 0$. For comparative analysis, two types of carbon nanotubes are considered, i.e., single- and multiple-wall CNTs. Moreover, water and kerosene oil are taken as the base fluids. The freestream velocity is taken as $\bar{U}_e(x) = a\bar{x}$, and velocity of stretching sheet is $\bar{U}_w(x) = c\bar{x}$, where a and c are the positive constants. Additionally, an induced magnetic field vector $(\bar{H})$ is presented by $\overline{H}_e(x) = H_0\bar{x}$ with two parallel and normal components say $\bar{H}_1$ and $\bar{H}_2$, where the uniform magnetic field H_0 is imposed parallel to the plate and external to the boundary layer in the direction of $\bar{x}$-axis. The induced magnetic field of normal components $\bar{H}_2$ vanishes at the wall with the parallel components $\bar{H}_1$ and approaching the imposed magnetic field value of H_0 at the edge of the boundary layer. T_w is the prescribed surface temperature and T_∞ is the ambient temperature. Moreover, φ_w and φ_∞ are the nano particle volume fraction at the surface and ambient values of nanoparticle volume fraction, respectively. The physical flow model is presented in Fig. 1.

The appropriate boundary-layer equations governing the stagnation point flow and heat transfer in electrically conducting viscous fluid containing carbon nanotubes (CNTs), following Iqbal et al. [50] and Gireesha et al. [51], can be shown to take the form

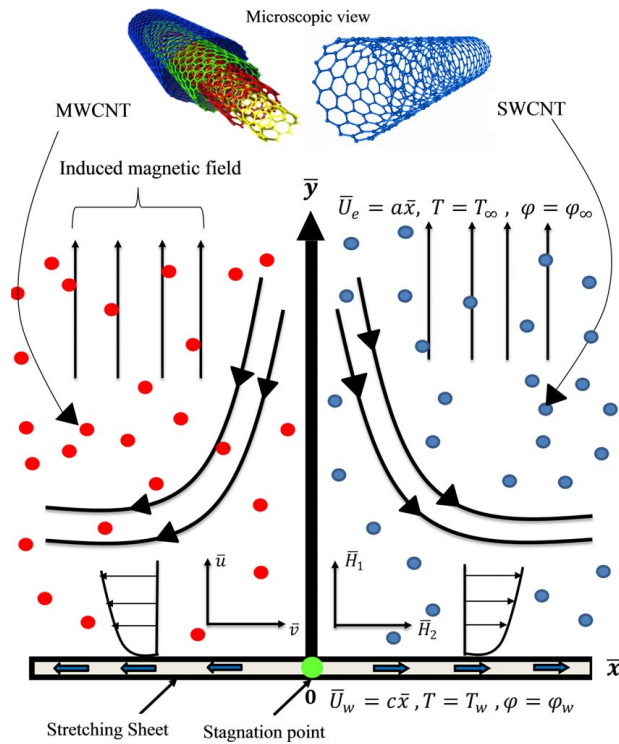$$\frac{\partial \bar{u}}{\partial \bar{x}} + \frac{\partial \bar{v}}{\partial \bar{y}} = 0 \tag{1}$$

Fig. 1 Physical model for magnetic induction CNT nanofluid stagnation flow from a stretching sheet

$$\frac{\partial \overline{H_1}}{\partial \bar{x}} + \frac{\partial \overline{H_2}}{\partial \bar{y}} = 0 \qquad (2)$$

$$\bar{u}\frac{\partial \bar{u}}{\partial \bar{x}} + \bar{v}\frac{\partial \bar{u}}{\partial \bar{y}} = \frac{\mu}{4\pi\rho_f}\left(\overline{H_1}\frac{\partial \overline{H_1}}{\partial \bar{x}} + \overline{H_2}\frac{\partial \overline{H_2}}{\partial \bar{y}}\right) + \left(\bar{U}_e\frac{d\bar{U}_e}{d\bar{x}} - \frac{\mu\overline{H_e}}{4\pi\rho_f}\frac{d\overline{H_e}}{d\bar{x}}\right)$$
$$+ \left(\frac{\mu_{nf}}{\rho_{nf}}\right)\frac{\partial^2 \bar{u}}{\partial \bar{y}^2} \qquad (3)$$

$$\bar{u}\frac{\partial \overline{H_1}}{\partial \bar{x}} + \bar{v}\frac{\partial \overline{H_1}}{\partial \bar{y}} - \left(\overline{H_1}\frac{\partial \bar{u}}{\partial \bar{x}} + \bar{H}_2\frac{\partial \bar{u}}{\partial \bar{y}}\right) = \mu_e\frac{\partial^2 \overline{H_1}}{\partial \bar{y}^2} \qquad (4)$$

$$(\rho C_p)_{nf}\left(\bar{u}\frac{\partial T}{\partial \bar{x}} + \bar{v}\frac{\partial T}{\partial \bar{y}}\right) = k_{nf}\frac{\partial^2 T}{\partial \bar{y}^2} \qquad (5)$$

The effective properties of nanofluids are defined mathematically as follows:

$$\mu_{nf} = \frac{\mu_f}{(1-\varphi)^{2.5}}, \qquad \rho_{nf} = (1-\varphi)\rho_f + \varphi\rho_{CNT}$$
$$(\rho c_p)_{nf} = (1-\varphi)(\rho c_p)_f + \varphi(\rho c_p)_{CNT}, \qquad \nu_{nf} = \frac{\mu_{nf}}{\rho_{nf}} \qquad (6)$$

The prescribe corresponding boundary conditions:

$$\overline{u} = \overline{U_w} = c\bar{x}, \quad \bar{v} = 0, \quad T = T_\infty, \quad \frac{\partial \overline{H_1}}{\partial \bar{y}} = \overline{H_2} = 0 \text{ as } \bar{y} = 0$$

$$\bar{u} \to \overline{U_e} = a\bar{x}, \quad T \to T_\infty, \quad \bar{H}_1 = \bar{H}_e(x) \to H_0\bar{x} \text{ as } \bar{y} \to \infty \qquad (7)$$

Here, $\bar{u}$, $\bar{v}$, $\bar{H}_1$, and $\bar{H}_2$ are velocity and magnetic field components along the $\bar{x}-$ and $\bar{y}-$ directions, respectively. Here, μ denotes the magnetic permeability and μ_e denotes the magnetic

diffusivity where $\mu_e = \frac{1}{4\pi\sigma\mu}$. T is the fluid temperature; ρ_{nf}, μ_{nf} are density and dynamic viscosity, respectively, of the magnetic CNT nanofluid. φ is the particle volume fraction parameter; ρ_f and ρ_{CNT} are density of fluid and carbon nanotube (CNT), respectively. $(c_p)_{nf}$, $(c_p)_f$, and $(c_p)_{CNT}$ are specific heat of nanofluid, base fluid, and CNTs. k_{nf}, k_f, and k_{CNT} are thermal conductivities of nanofluid, base fluid, and the CNTs respectively.

Theoretical Models for Effective Thermal Conductivity. Many robust theoretical models are available for estimating the effective thermal conductivity amplification of CNTs. Following Maxwell [52], we define

$$\frac{k_{CNT}}{k_f} = 1 + \frac{3(\alpha - 1)\varphi}{(\alpha + 2) + (\alpha - 1)\varphi} \qquad (8)$$

In the light of higher orders of volume fraction, Jeffery [53] and Davis [54] have proposed the following theoretical models:

$$\frac{k_{nf}}{k_f} = 1 + 3\lambda\varphi + \left(3\lambda^2 + \frac{3\lambda^2}{4} + \frac{9\lambda^2}{16}\frac{\alpha + 2}{2\alpha + 3} + \cdots\right)\varphi^2 \qquad (9)$$

and

$$\frac{k_{nf}}{k_f} = 1 + \frac{3(\alpha - 1)\varphi}{(\alpha + 2) + (\alpha - 1)\varphi}\{\varphi + \varphi(\alpha)\,\varphi^2 + O(\varphi^3)\} \qquad (10)$$

respectively, where $\lambda = (\alpha - 1)/(\alpha + 2)$.

Here, α is the ratio of thermal conductivity.

To deal with the geometry, i.e., shape factor of the particles, Hamilton and Crosser [55] developed the following theoretical model for heterogenous two-component suspensions:

$$\frac{k_{nf}}{k_f} = \frac{\alpha + (n - 1) - (n - 1)(1 - \alpha)\phi}{\alpha + (n - 1) + (1 - \alpha)\phi} \qquad (11)$$

where n is the shape factor of a particle given by $n = 3/\varphi^\omega$, $\varphi = 1$ for spheres and 0.5 for cylinders and ω ranges from 1 to 2. Based on Maxwell theory and taking into account the rotational elliptical nanotubes, as considered by Xue [56] have proposed the following relation:

$$\frac{k_{nf}}{k_f} = \frac{1 - \phi + 2\phi\,\dfrac{k_{CNT}}{k_{CNT} - k_f}\ln\dfrac{k_{CNT} + k_f}{2k_f}}{1 - \phi + 2\phi\,\dfrac{k_f}{k_{CNT} - k_f}\ln\dfrac{k_{CNT} + k_f}{2k_f}} \qquad (12)$$

In the current study, the Xue model [56] is employed to evaluate the thermal conductivity and the dimensionless heat transfer rates of CNT nanofluids.

3 Transformation of Model

In primitive variables, the conservation Eqs. (1)–(5), and boundary conditions (7), while well-posed, remain very challenging to solve, even numerically. Therefore, following Hamad [57], the following non-dimensional variables are introduced:

$$x = \frac{\bar{x}}{\sqrt{\frac{\nu_f}{c}}}, \quad y = \frac{\bar{y}}{\sqrt{\frac{\nu_f}{c}}}, \quad u = \frac{\bar{u}}{\sqrt{c\nu_f}}, \quad v = \frac{\bar{v}}{\sqrt{c\nu_f}},$$
$$\theta = \frac{T - T_\infty}{T_w - T_\infty} \quad H_1 = \frac{\overline{H_1}}{H_0\sqrt{\frac{\nu_f}{c}}}, \quad H_2 = \frac{\overline{H_2}}{H_0\sqrt{\frac{\nu_f}{c}}} \qquad (13)$$

The governing equations are thereby rendered into non-dimensional form, as follows:

$$\frac{\partial u}{\partial x} + \frac{\partial v}{\partial y} = 0 \qquad (14)$$

$$\frac{\partial H_1}{\partial x} + \frac{\partial H_2}{\partial y} = 0 \tag{15}$$

$$\left(1 - \varphi + \varphi\frac{\rho_{CNT}}{\rho_f}\right)\left(u\frac{\partial u}{\partial x} + v\frac{\partial u}{\partial y}\right) = \left(1 - \varphi + \varphi\frac{\rho_{CNT}}{\rho_f}\right)$$
$$\left[\frac{\mu}{4\pi\rho_f}\frac{H_0^2}{c^2}\left(H_1\frac{\partial H_1}{\partial x} + H_2\frac{\partial H_2}{\partial y} - x\right) + \frac{a^2}{c^2}x\right] + \frac{1}{(1-\varphi)^{2.5}}\frac{\partial^2 u}{\partial y^2} \tag{16}$$

$$u\frac{\partial H_1}{\partial x} + v\frac{\partial H_1}{\partial y} - H_1\frac{\partial u}{\partial x} - H_2\frac{\partial u}{\partial y} = \frac{\mu_e}{\nu_f}\frac{\partial^2 H_1}{\partial y^2} \tag{17}$$

$$u\frac{\partial\theta}{\partial x} + v\frac{\partial\theta}{\partial y} = \frac{k_{nf}}{\nu_f(\rho C_p)_{nf}} \cdot \frac{\partial^2\theta}{\partial y^2} \tag{18}$$

Here, ν_f refers to kinematic viscosity of the base fluid where $\upsilon_f = \mu_f/\rho_f$.

The dimensionless boundary conditions emerge as

$$u = U_w = x, \quad v = 0, \quad \theta = 1, \quad \frac{\partial H_1}{\partial y} = H_2 = 0 \text{ at } y = 0$$
$$u \to U_e = \frac{a}{c}x, \quad \theta = 0, \quad H_1 = H_e(x) \to x \text{ as } y \to \infty \tag{19}$$

Proceeding with the analysis, the dimensional momentum and magnetic stream functions ψ_1 and ψ_2 are defined as follows:

$$u = \frac{\partial\psi_1}{\partial y} \text{ and } v = -\frac{\partial\psi_1}{\partial x} \tag{20}$$

$$H_1 = \frac{\partial\psi_2}{\partial y} \text{ and } H_2 = -\frac{\partial\psi_2}{\partial x} \tag{21}$$

Implementing Eqs. (20) and (21) in Eqs. (14)–(19) leads to

$$\left(1 - \varphi + \varphi\frac{\rho_{CNT}}{\rho_f}\right)\left(\frac{\partial\psi_1}{\partial y}\frac{\partial^2\psi_1}{\partial x\partial y} - \frac{\partial\psi_1}{\partial x}\frac{\partial^2\psi_1}{\partial y^2}\right) = \left(1 - \varphi + \varphi\frac{\rho_{CNT}}{\rho_f}\right)$$
$$\left[\frac{\mu}{4\pi\rho_f}\frac{H_0^2}{c^2}\left(\frac{\partial\psi_2}{\partial y}\frac{\partial^2\psi_2}{\partial x\partial y} - \frac{\partial\psi_2}{\partial x}\frac{\partial^2\psi_2}{\partial y^2} - x\right) + \frac{a^2}{c^2}x\right] + \frac{1}{(1-\varphi)^{2.5}}\frac{\partial^3\psi_1}{\partial y^3} \tag{22}$$

$$\frac{\partial\psi_1}{\partial y}\frac{\partial^2\psi_2}{\partial x\partial y} - \frac{\partial\psi_1}{\partial x}\frac{\partial^2\psi_2}{\partial y^2} - \frac{\partial\psi_2}{\partial y}\frac{\partial^2\psi_1}{\partial x\partial y} + \frac{\partial\psi_2}{\partial x}\frac{\partial^2\psi_1}{\partial y^2} = \frac{\mu_e}{\nu_f}\frac{\partial^3\psi_2}{\partial y^3} \tag{23}$$

$$\left(1 - \varphi + \varphi\frac{(\rho C_p)_{CNT}}{(\rho C_p)_f}\right)\left(\frac{\partial\psi_1}{\partial y}\frac{\partial\theta}{\partial x} - \frac{\partial\psi_1}{\partial x}\frac{\partial\theta}{\partial y}\right)$$
$$= \frac{k_{nf}}{k_f} \cdot \frac{k_f}{\nu_f(\rho C_p)_{nf}}\frac{\partial^2\theta}{\partial y^2} \tag{24}$$

The corresponding boundary conditions are

$$\frac{\partial\psi_1}{\partial y} = x, \quad -\frac{\partial\psi_1}{\partial x} = 0, \quad \theta = 1, \quad -\frac{\partial\psi_2}{\partial x} = 0, \quad \frac{\partial^2\psi_2}{\partial y^2} = 0 \text{ at } y = 0$$
$$\frac{\partial\psi_1}{\partial y} = \frac{a}{c}x, \quad \theta = 0, \quad \frac{\partial\psi_2}{\partial y} = x \text{ as } y \to \infty \tag{25}$$

Lie-Group Scaling Transformations. The transformed system (Eqs. (22)–(25)) can be further modified via application of a simplified form of Lie-group transformations namely, the scaling group of transformations, which are described extensively by Ibrahim et al. [58], Mukhopadhyay et al. [59], Kandasamy and Muhaimin [60], Muhaimin et al. [61], and Hamad and Pop [62]). In line with these studies, we implement the following transformations:

$$\eta = y, \quad \psi_1 = xf(\eta), \quad \theta = \theta(\eta), \quad \psi_2 = xg(\eta) \tag{26}$$

The nonlinear boundary value problem defined by Eqs. (22)–(25) is therefore reduced to the following system of coupled nonlinear ordinary differential equations and boundary conditions:

$$\frac{1}{(1-\varphi)^{2.5}}f''' - \left(1 - \varphi + \varphi\frac{\rho_{CNT}}{\rho_f}\right)[f'^2 - ff'' - \beta(g'^2 - gg'' - 1) - A^2] = 0 \tag{27}$$

$$\lambda g''' + f.g'' - g.f'' = 0 \tag{28}$$

$$\frac{k_{nf}}{k_f}\theta'' + Pr\left(1 - \varphi + \varphi\frac{(\rho C_p)_{CNT}}{(\rho C_p)_f}\right)f.\theta' = 0 \tag{29}$$

$$f'(\eta) = 1, f(\eta) = 0, g(\eta) = 0, g''(\eta) = 0, \theta(\eta) = 1 \text{ at } \eta = 0$$
$$f'(\eta) = A, g'(\eta) = 1, \theta(\eta) = 0 \text{ as } \eta \to \infty \tag{30}$$

In the above-mentioned formulations, prime indicates differentiation with respect to η. Moreover, Prandtl number (Pr), stretching rate ratio parameter (A), reciprocal of magnetic Prandtl number (λ), and magnetic body force parameter (β) are defined as follows: Prandtl number $Pr = \frac{(\mu c_p)_f}{k_f}$; reciprocal of magnetic Prandtl number $\lambda = \frac{\mu_e}{\nu_f}$; magnetic body force parameter $\beta = \frac{\mu}{4\pi\rho_f}\frac{H_0^2}{c^2}$; and stretching sheet ratio parameter $A = \frac{a}{c}$. It is further noteworthy that $A = \frac{a}{c}$ is the ratio of the surface velocity to the freestream fluid velocity and $A > 0$ corresponds to the situation when the surface moves in same direction to the freestream whereas $A < 0$ implies that the surface moves in the opposite direction to the freestream. The case $A = 0$ is associated with a fixed surface. A key objective of the current investigation is the numerical determination of any possible dual solutions for certain values of β and λ within the range of stretching rate ratio parameter. Thereafter, the stable and unstable solutions may be analyzed graphically. A comprehensive numerical study of the effects of all key parameters on velocity, temperature, and induced magnetic field distributions for both SWCNT and MWCNT nanofluids is also conducted. Furthermore, in materials processing fluid dynamics, the wall gradient quantities of physical interest are the local skin friction coefficient C_{f_x} and the local rate of heat transfer coefficient Nu_x, i.e., local Nusselt number. These non-dimensional functions are defined, respectively, as follows [57]:

$$C_f = \frac{\tau_w}{\frac{1}{2}\rho_\infty\bar{u}_\infty^2} \tag{31}$$

$$N_u = \frac{\bar{x}q_w}{k_f(T_w - T_\infty)} \tag{32}$$

Here, τ_w and q_w are the dimensional wall shear stress and wall heat flux which are respectively defined as

$$\tau_w = \mu_{nf}\left(\frac{\partial\bar{u}}{\partial\bar{y}}\right)_{\bar{y}=0} \tag{33}$$

$$q_w = -k_{nf}\left(\frac{\partial T}{\partial \bar{y}}\right)_{\bar{y}=0} \tag{34}$$

In the absence of nanoscale and induced magnetic field effects, the dimensionless momentum Eq. (27) with respect to the contracted boundary condition Eq. (30) is reduced to that of Crane [10] who presented the closed form solution as follows:

$$f(\eta) = 1 - e^{-\eta} \tag{35}$$

The relevant non-dimensional velocity components are

$$u = \frac{\partial \psi_1}{\partial y} = x f'(\eta) = x e^{-y} \tag{36}$$

$$v = -\frac{\partial \psi_1}{\partial x} = -f(\eta) = e^{-y} - 1 \tag{37}$$

The dimensional velocity components are

$$\bar{u} = c\bar{x} e^{-\bar{y}\sqrt{\frac{c}{\nu_f}}} \tag{38}$$

$$\bar{v} = \sqrt{c\nu_f}\left(e^{-\bar{y}\sqrt{\frac{c}{\nu_f}}} - 1\right) \tag{39}$$

Since $f'(\eta) = -e^{\eta}$, it follows that

$$f''(\eta) = -e^{-\eta} = -e^{-\bar{y}} = -e^{-\bar{y}\sqrt{\frac{c}{\nu_f}}} \tag{40}$$

For the present study, the shear stress at the stretching sheet characterized by the skin friction coefficient is obtained as follows:

$$C_f = \frac{\mu_{nf}\left(\frac{\partial \bar{u}}{\partial \bar{y}}\right)_{y=0}}{\rho_f \bar{U}_w^2} = \frac{1}{(1-\varphi)^{2.5}} \operatorname{Re}_x^{-\frac{1}{2}} f''(0) \tag{41}$$

Algebraic transposition gives the required non-dimensional form as

$$\operatorname{Re}_x^{\frac{1}{2}} C_f = \frac{1}{(1-\varphi)^{2.5}} f''(0) \tag{42}$$

Now, the wall heat transfer rate at the stretching sheet characterized by the Nusselt number Nu_x is given by

$$\operatorname{Nu} = \frac{-\bar{x} k_{nf}\left(\frac{\partial T}{\partial \bar{y}}\right)_{y=0}}{k_f(T_w - T_\infty)} = -\frac{k_{nf}}{k_f} \operatorname{Re}_x^{\frac{1}{2}} \theta'(0) \tag{43}$$

The required non-dimensional form is given by

$$\operatorname{Re}_x^{-\frac{1}{2}} \operatorname{Nu}_x = -\frac{k_{nf}}{k_f} \theta'(0) \tag{44}$$

Here, $\operatorname{Re}_x = \frac{\bar{U}_w \bar{x}}{\nu_f}$ is the local Reynolds number.

4 MATLAB Numerical Computation

The system of ordinary differential Eqs. (27)–(29) with boundary conditions Eq. (30) has been solved by MATLAB software using the bvp4c function [63]. This procedure requires conversion of the *higher* order nonlinear ordinary differential equations into *first-order* ordinary differential equations. With experimentation of initial guesses for f', f, θ, θ', g, g', it is possible to determine the first and second solutions. Equations (27)–(29) are converted to

$$f''' = (1-\varphi)^{2.5}\left(1 - \varphi + \varphi\frac{\rho_{CNT}}{\rho_f}\right)[f'^2 - ff'' - \beta(g'^2 - gg'' - 1) - A^2] \tag{45}$$

$$g''' = \frac{1}{\lambda}(g.f'' - f.g'') \tag{46}$$

$$\theta'' = -\frac{k_f}{k_{nf}} Pr\left(1 - \varphi + \varphi\frac{(\rho C_p)_{CNT}}{(\rho C_p)_f}\right) f.\theta' \tag{47}$$

The collective eighth-order system of Eqs. (45)–(47) are next transformed into eight first-order differential equations. Letting $\eta = z$ and defining the following substitutions:

$$y_1 = f, \ y_2 = f', \ y_3 = f'', \ y_4 = g \tag{48}$$

$$y_5 = g', \ y_6 = g'', \ y_7 = \theta, \ y_8 = \theta' \tag{49}$$

The corresponding octad of first-order differential equations is

$$\frac{dy_1}{dz} = y_2 = f' \tag{50}$$

$$\frac{dy_2}{dz} = y_3 = f'' \tag{51}$$

$$\frac{dy_3}{dz} = f'''$$
$$= (1-\varphi)^{2.5}\left(1 - \varphi + \varphi\frac{\rho_{CNT}}{\rho_f}\right)[y_2^2 - y_1 y_3 - \beta(y_5^2 - y_4 y_6 - 1) - A^2] \tag{52}$$

$$\frac{dy_4}{dz} = y_5 = g' \tag{53}$$

$$\frac{dy_5}{dz} = y_6 = g'' \tag{54}$$

$$\frac{dy_6}{dz} = g''' = \frac{1}{\lambda}(y_3 y_4 - y_1 y_6) \tag{55}$$

$$\frac{dy_7}{dz} = y_8 = \theta \tag{56}$$

$$\frac{dy_8}{dz} = \theta'' = -\frac{k_f}{k_{nf}} Pr\left(1 - \varphi + \varphi\frac{(\rho C_p)_{CNT}}{(\rho C_p)_f}\right) y_1 y_8 \tag{57}$$

The boundary conditions (Eq. (30)) are next transformed, for which ya denotes the left boundary and yb be the right boundary

$$
\begin{array}{ll}
ya(1) = 0 & yb(2) - A = 0 \\
ya(3) - 1 = 0 & yb(4) - 1 = 0 \\
ya(5) = 0 & yb(6) = 0 \\
ya(7) = 0 & ya(8) - 1 = 0
\end{array} \tag{58}
$$

5 Data, Numerical Validation, and Results

5.1 Data. Numerical calculations have been carried out for different values of the control parameters. Thermophysical properties of base fluids and CNTs are given in Tables 1 and 2 providing the data for all relevant thermophysical properties of nanofluids with solid volume fraction of CNTs.

The Prandtl number for water-based CNTs and kerosene-oil-based CNTs are considered constant in the simulations

$$\text{For water, } \operatorname{Pr} = \frac{(\mu C_p)_f}{k_f} = \frac{8.90 \times 10^{-4} \text{kgm}^{-1}\text{s}^{-1} \times 4179 \text{jkg}^{-1}\text{K}^{-1}}{0.613 \text{Wm}^{-1}\text{K}^{-1}} \approx 6.2$$

Table 1 Thermophysical properties of CNTs [29]

Physical properties	Water	Base fluid Kerosene oil	Nanoparticles SWCNT	Nanoparticles MWCNT
ρ (kg m^{-3})	997	783	2600	1600
C_p (J kg^{-1} K^{-1})	4179	2090	425	796
k (W m^{-1} K^{-1})	0.613	0.145	6600	3000

$$\text{For kerosene oil, Pr} = \frac{(\mu C_p)_f}{k_f}$$

$$= \frac{1.45 \times 10^{-3}\,\text{kgm}^{-1}\text{s}^{-1} \times 2090\,\text{jkg}^{-1}\text{K}^{-1}}{0.145\,\text{Wm}^{-1}\text{K}^{-1}} \approx 21.0$$

The range of nanoparticle volume fraction φ is considered from 0 to 0.2 where $\varphi = 0$ corresponding to a regular viscous fluid [29]. The stretching sheet ratio parameter, A, is prescribed values of $A = 0.5$, 0.8, 1.2, 1.5 [50]. The value of reciprocal of magnetic Prandtl number is $\lambda = 0.5, 1, 5, 10$ [52]. The value of magnetic parameter β is taken equal to $\beta = 0.1, 0.2, 1, 1.5, 2.5$ [63]. The case $\beta = 0$ corresponds to the flow of nanofluid in the absence of induced magnetic field.

5.2 Validation. The validation of the MATLAB code is conducted by comparing it with previously published studies. Here, the accuracy of the results is represented by Table 3 which compares the reduced skin friction $f''(0)$ for the range $0.1 \leq A \leq 1.0$ and $\varphi = \beta = 0$ with the homotopy solutions obtained by Hayat et al. [64], Hayat et al. [65] and Iqbal et al. [50]. Very good agreement is achieved testifying to the accuracy of the MATLAB bvp4c solutions.

Table 4 shows the comparison of skin friction coefficient, and Table 5 documents the comparisons for heat transfer coefficient for both water- and kerosene-oil-based SWCNT- and MWCNT nanofluids for the range of parameters $0 \leq \varphi \leq 0.2$.

5.3 Skin Friction Analysis. The impact of magnetic parameter, β, on the reduced skin friction for water- and kerosene-based SWCNT with keeping other parameters fixed is visualized in Figs. 2–5. These figures show that dual solutions exist when $A > A_c$ for both water- and kerosene-based SWCNT and MWCNT. However, no solutions are found to exist when $A < A_c$, indicating that there is boundary-layer separation, and therefore, laminar boundary-layer approximations are not physically realizable. Figures 2 and 3 display the variation in reduced skin friction $f''(0)$ of water-based SWCNT nanofluid and MWCNT nanofluid, respectively, as a function of stretching rate ratio parameter (A) for representative values of β when $Pr = 6.2$, $\lambda = 0.5$, and $\varphi = 0.2$.

Table 3 Comparison of values of skin friction with those of Hayat et al. [64], Hayat et al. [65], and Iqbal et al. [50] for different values of $A = a/c$ when $\phi = \beta = 0$

A	Present study (first solution)	Present study (second solution)	Hayat et al. [64]	Hayat et al. [65]	Iqbal et al. [50]
0.1	−0.969656	−1.220800	−0.96939	−0.96937	−0.969386
0.2	−0.918165	−1.215516	−0.91811	−0.91813	−0.918107
0.5	−0.667264	−1.086370	−0.66726	−0.66723	−0.667263
0.7	−0.433476	−0.899362	−0.43346	−0.43345	−0.433475
0.8	−0.299389	−0.779299	−0.29929	−0.29921	−0.299388
0.9	−0.154717	−0.644787	−0.15458	−0.154571	−0.154716
1.0	−0.00000	−0.498013	−0.00000	−0.000000	−0.000000

Figure 2 shows that for magnetic parameter $\beta = 0.2$, the critical value determined is $A_c = -1.02$. It is observed that when the magnetic parameter β increases, i.e., $\beta = 0.5$, the range of A_c values where solutions exist is shrinking ($A > A_c = -0.82$) for water-based SWCNT nanofluid. For further increment in the magnetic parameter $\beta = 1$, the range becomes $A > A_c = -0.46$. So the study implies that when the magnetic effect occurring at the boundary increases, the range of A_c values for the existence of the solutions becomes smaller. Evidently, with the increase in magnetic parameter β the reduced skin friction strongly decreases (values are more negative) for water-based SWCNT. In Fig. 3, the value of the magnetic parameter $\beta = 0.2$ produces a critical value $A_c = -1.05$, and when the magnetic parameter β increases from 0.2 to 0.5, the range of A_c values where solutions exist is again shrank ($A > A_c = -0.83$) for water-based MWCNT-nanofluid. For further increment in the magnetic parameter $\beta = 1$, the range becomes $A > A_c = -0.49$.

Therefore, the reduced skin friction *decreases* (values are increasingly negative) for water-based SWCNT-nanofluid with elevation in magnetic parameter β due to an increase of magnetic effect again due to modification in the magnetic force acting, leading to deceleration. It is concluded that SWCNT-nanofluid has higher reduced skin friction as compared to MWCNT-nanofluid for water.

Figures 4 and 5 display the reduced skin friction $f''(0)$ of kerosene-oil-based SWCNT and MWCNT, respectively, as a function of the stretching rate ratio parameter (A) for representative values of β when $Pr = 21$, $\lambda = 0.5$, and $\varphi = 0.2$. In Fig. 4, for the value of magnetic parameter $\beta = 0.2$, a critical value $A_c = -0.43$ is computed. It is observed that when the magnetic parameter β increases, i.e, $\beta = 0.5$, the range of A_c values where solutions exist is compressed ($A > A_c = -0.41$) for kerosene-based SWCNT-nanofluid.

For further increment in the magnetic parameter $\beta = 1$, the range is decreased and becomes $A > A_c = -0.39$. Clearly with an elevation in magnetic parameter β, the reduced skin friction is strongly modified for kerosene-oil-based SWCNT. In Fig. 5 for a value of

Table 2 Variation of thermophysical properties of nanofluids with solid volume fraction [29]

SWCNT	φ	ρ (kgm^{-3})	ρC_p ($\times 10^6$) (J m^{-3} K^{-1})	k (W m^{-1} K^{-1})	MWCNT	φ	ρ (kgm^{-3})	ρC_p ($\times 10^6$) (J m^{-3} K^{-1})	K (Wm^{-1} K^{-1})
Water	0	997	4.167	0.613	Water	0	997	4.167	0.613
	0.04	1,061	4.044	1.051		0.04	1,021	4.051	1.011
	0.08	1,125	3.921	1.528		0.08	1,045	3.935	1.444
	0.12	1,189	3.799	2.048		0.12	1,069	3.819	1.916
	0.16	1,253	3.676	2.618		0.16	1,093	3.703	2.434
	0.20	1,317	3.554	3.245		0.20	1,117	3.588	3.002
Kerosene	0	783	1.636	0.150	Kerosene	0	783	1.636	0.150
	0.04	855	1.615	0.274		0.04	815	1.621	0.265
	0.08	928	1.593	0.410		0.08	848	1.607	0.390
	0.12	1,001	1.572	0.559		0.12	881	1.592	0.526
	0.16	1,073	1.551	0.721		0.16	913	1.578	0.676
	0.20	1,146	1.530	0.899		0.20	946	1.563	0.840

Table 4 Comparison of reduced skin friction $f'(0)$ of water and kerosene-based SWCNT and MWCNT for different values of solid volume fraction (φ) when $Pr = 6.2$(water), $Pr = 21$ (kerosene oil), $A = 0.5$, $\lambda = 1$, and $\beta = 0.1$

	φ	A	Present study (first solution)	Present study (second solution)	Iqbal et al. [50] (first solution)
Water based					
SWCNT	0	0.3	−0.343850	−1.255369	−0.343865
		0.5	−0.560774	−1.164244	−0.560864
	0.1	0.3	−0.324458	−1.222000	−0.324138
		0.5	−0.527617	−1.142609	−0.527603
	0.2	0.3	−0.298987	−1.185087	−0.298900
		0.5	−0.483232	−1.120913	−0.483275
Water based					
MWCNT	0	0.3	−0.343850	−1.255369	−0.343865
		0.5	−0.560774	−1.164244	−0.560864
	0.1	0.3	−0.309880	−1.200090	−0.309852
		0.5	−0.502356	−1.129283	−0.502776
	0.2	0.3	−0.277014	−1.161866	−0.277013
		0.5	−0.442993	−1.111114	−0.442926
Kerosene based					
SWCNT	0	0.3	−0.343850	−1.255369	−0.343866
		0.5	−0.560774	−1.164244	−0.560864
	0.1	0.3	−0.334180	−1.238617	−0.334182
		0.5	−0.544630	−1.168384	−0.544676
	0.2	0.3	−0.314170	−1.206467	−0.314171
		0.5	−0.510357	−1.133056	−0.510350
Kerosene based					
MWCNT	0	0.3	−0.343850	−1.255369	−0.343865
		0.5	−0.560774	−1.164244	−0.560864
	0.1	0.3	−0.316174	−1.209421	−0.316122
		0.5	−0.513734	−1.134837	−0.513752
	0.2	0.3	−0.497280	−1.170759	−0.497279
		0.5	−0.474860	−1.114072	−0.474859

Table 5 Comparison of reduced heat transfer $-\theta'(0)$ of water- and kerosene-based SWCNT and MWCNT for different values of solid volume fraction (φ) when $Pr = 6.2$ (water), $Pr = 21$ (kerosene oil), $A = 0.5$, $\lambda = 1$, and $\beta = 0.1$

	φ	A	Present study (first solution)	Present study (second solution)	Iqbal et al. [50] (first solution)
Water based					
SWCNT	0	0.3	1.921848	0.139148	1.921850
		0.5	1.879745	0.002125	1.879738
	0.1	0.3	1.063675	0.250763	1.063670
		0.5	1.028441	0.104320	1.028429
	0.2	0.3	0.745427	0.209906	0.745134
		0.5	0.717252	0.150600	0.717276
Water based					
MWCNT	0	0.3	1.921848	0.139148	1.921850
		0.5	1.879745	0.002125	1.879738
	0.1	0.3	1.103179	0.178497	1.103134
		0.5	1.069269	0.059675	1.069222
	0.2	0.3	0.783059	0.146797	0.783088
		0.5	0.756865	0.091991	0.756862
Kerosene based					
SWCNT	0	0.3	3.587979	0.000086	3.587933
		0.5	3.543657	0.000000	3.543653
	0.1	0.3	1.937916	0.066138	1.937945
		0.5	1.896988	0.000860	1.896922
	0.2	0.3	1.383338	0.110898	1.3833123
		0.5	1.347040	0.014326	1.347222
Kerosene based					
MWCNT	0	0.3	3.587979	0.000086	3.587933
		0.5	3.543657	0.000000	3.543653
	0.1	0.3	2.008121	0.008361	2.008445
		0.5	1.969463	0.000071	1.969732
	0.2	0.3	1.453111	0.012009	1.453110
		0.5	1.420414	0.001047	1.420438

magnetic parameter $\beta = 0.2$, the critical value computed is $A_c = -0.80$, and when the magnetic parameter β increases from 0.2 to 0.5, the range of A_c values where solutions exist becomes reduced ($A > A_c = -0.78$) for kerosene-oil-based MWCNT. For further enhancement in the magnetic parameter $\beta = 1$, the range becomes $A > A_c = -0.75$. So, it is apparent from the figures that the reduced skin friction decreases for kerosene-oil-based MWCNT with an increase in magnetic parameter β. So, the analysis further indicates that when the magnetic effect occurs at the boundary, the resistance between the fluid and the plate decreases, accelerating the boundary-layer separation, and it happens in the range where the dual solution exists. The boundary layer accelerates more with the growing magnetic effect. Moreover, from these figures, it is noticed that the existence of a dual solution takes place when $A > A_c$, which indicates a physically unrealizable boundary-layer separation and boundary-layer approximation.

Again, this is due to adjustment in magnetic body force with the stronger magnetic field, as simulated in the induction modified term, $-\beta(g'^2 - gg'' - 1)$ appearing in the momentum Eq. (27). Overall, SWCNT-nanofluid, however, achieves higher magnitudes of reduced skin friction as compared to MWCNT-nanofluid for kerosene oil. On the other hand, kerosene oil CNT nanofluids attain higher skin friction as compared to water-based CNT nanofluids.

5.4 Heat Transfer Analysis. The influence of reciprocal magnetic Prandtl number λ on reduced heat transfer, i.e., Nusselt number function, $-\theta'(0)$, for water- and kerosene-oil-based SWCNT and MWCNT-nanofluids as a function of stretching rate ratio parameter (A) for representative values of β when $Pr = 6.2$, $\lambda = 0.5$, and $\varphi = 0.2$ is depicted in Figs. 6 and 7. These figures indicate that dual solutions exist when $A > A_c$ for both water- and

kerosene-based SWCNT and MWCNT nanofluids. However, no solutions are found to exist when $A < A_c$, and indicating the presence of *boundary-layer separation* for which the laminar boundary-layer approximations break down. Figure 6 shows that for reciprocal magnetic Prandtl number $\lambda = 1$, the critical value obtained is $A_c = 0.351$. With a higher reciprocal magnetic Prandtl number $\lambda = 5$, the range of A_c values where solutions exist are shrinking ($A > A_c = 0.398$) for water-based SWCNT-nanofluid. For further increment in the reciprocal magnetic Prandtl number
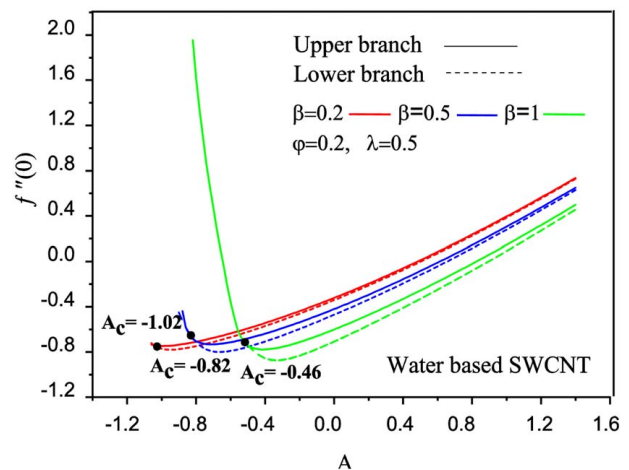

Fig. 2 Effects of β on reduced skin friction $f'(0)$ of water-based SWCNT-nanofluid as a function of stretching rate ratio parameter A when $Pr = 6.2$, $\lambda = 0.5$, and $\varphi = 0.2$
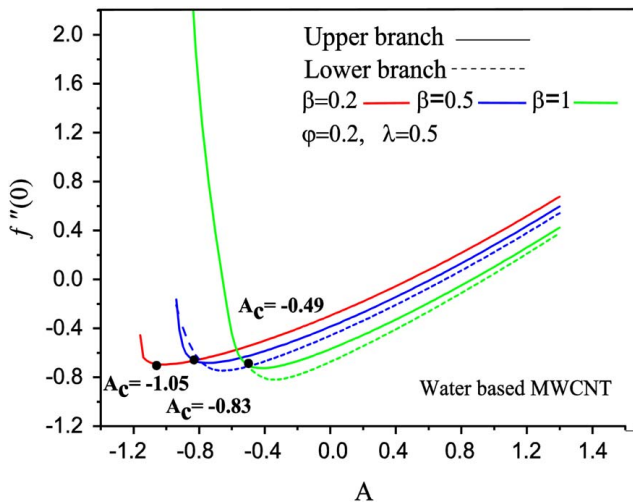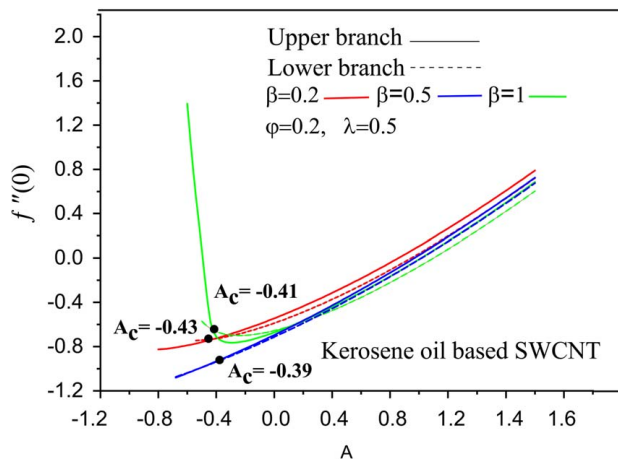
Fig. 3 Effects of β on reduced skin friction $f''(0)$ of water-based MWCNT-nanofluid as a function of stretching rate ratio parameter A when $Pr = 6.2$, $\lambda = 0.5$, and $\varphi = 0.2$

Fig. 5 Effects of β on reduced skin friction $f''(0)$ of kerosene-oil-based MWCNT as a function of stretching rate ratio parameter A when $Pr = 6.2$, $\lambda = 0.5$, and $\varphi = 0.2$

Fig. 4 Effects of β on reduced skin friction $f''(0)$ of kerosene-oil-based SWCNT as a function of stretching rate ratio parameter A when $Pr = 6.2$, $\lambda = 0.5$, and $\varphi = 0.2$

Fig. 6 Effects of λ on reduced heat transfer $-\theta'(0)$ of water-based SWCNT-nanofluid as a function stretching rate ratio parameter A when $Pr = 6.2$, $\beta = 0.2$, and $\varphi = 0.2$

$\lambda = 10$, the range compresses to $A > A_c = 0.451$. With elevation in reciprocal magnetic Prandtl number λ, the reduced heat transfer increases for water-based SWCNT. $\lambda = \dfrac{\mu_e}{\nu_f}$ and expresses the ratio of magnetic diffusion rate to viscous diffusion rate. The magnetic Reynolds number in the regime is adequately large to invoke magnetic induction. Magnetic Prandtl number quantifies the distortion in the induced magnetic field by the flow field. For cases where the magnetic Reynolds number is extremely small, there is no distortion in the magnetic field. For a reciprocal magnetic Prandtl number $\lambda = 1$, the actual magnetic Prandtl number is also 1 and viscous and magnetic diffusivities are equal. For $\lambda = 5$, the magnetic Prandtl number is 0.2, and therefore, the magnetic diffusion rate is five times greater than the viscous diffusion rate. This produces a much greater sensitivity in the magnetic induction field.

In Fig. 7, the value of reciprocal magnetic Prandtl number $\lambda = 1$ corresponds to a critical value of the sheet stretching rate parameter (A) of $A_c = 0.350$, and when the reciprocal magnetic Prandtl number increases to $\lambda = 5$, the range of A_c values where solutions exist is compressed ($A > A_c = 0.369$) for water-based MWCNT-nanofluids. For further enhancement in the reciprocal magnetic Prandtl number
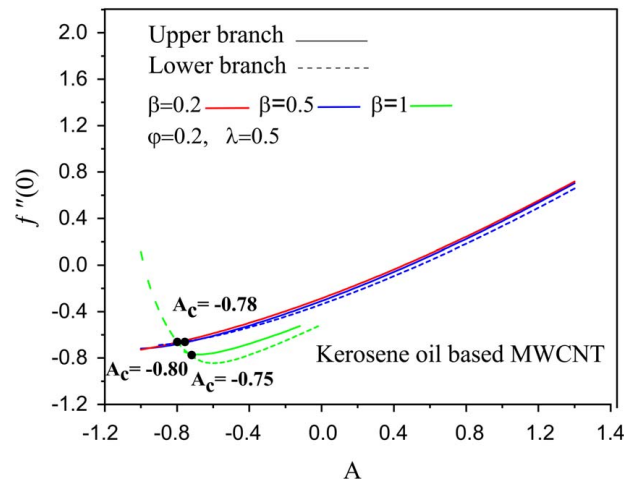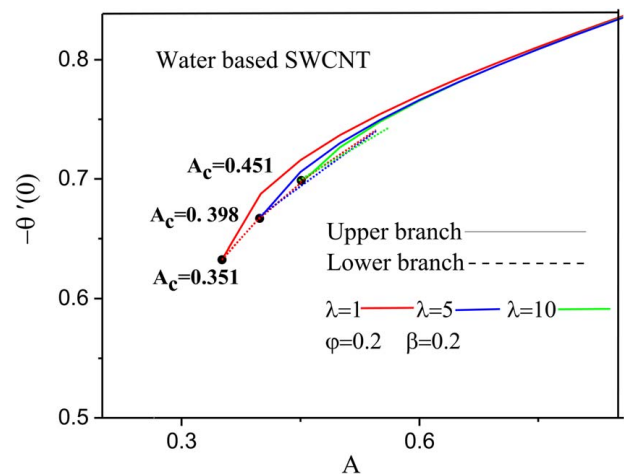
$\lambda = 10$, (i.e., actual magnetic Prandtl number of 0.1), the range becomes $A > A_c = 0.40$. With an increase in reciprocal magnetic Prandtl number λ, the reduced heat transfer is *slightly depleted* for water-based MWCNT. Reduced heat transfer rates are marginally greater for water SWCNT-nanofluids compared with water MWCNT-nanofluids.

Figures 8 and 9 display the reduced heat transfer $-\theta'(0)$ for kerosene-oil-based SWCNT and MWCNT-nanofluids, respectively, as a function of stretching rate ratio parameter (A) for representative values of reciprocal magnetic Prandtl number λ when $Pr = 21$, $\lambda = 0.5$, and $\varphi = 0.2$. From Fig. 8, the value of reciprocal magnetic Prandtl number $\lambda = 1$ produces a critical stretching parameter ratio value of $A_c = 0.301$. It is observed that when the magnetic Prandtl number λ increases, i.e., $\lambda = 5$, the range of A_c values where solutions exist becomes reduced ($A > A_c = 0.325$) for kerosene-oil-based SWCNT. For further increment in the magnetic Prandtl number $\lambda = 10$, the range contracted to $A > A_c = 0.398$.

Elevation in reciprocal magnetic Prandtl number λ results in reduced heat transfer decreasing for kerosene-oil-based SWCNT-nanofluids, since with stronger magnetic diffusivity there is greater conversion to heat in the boundary layer and an
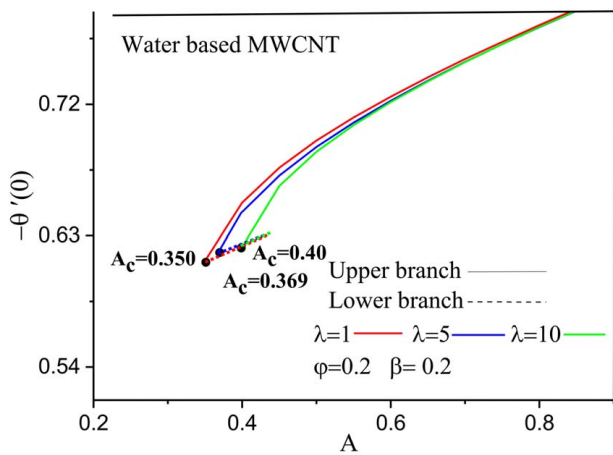
Fig. 7 Effects of λ on reduced heat transfer $-\theta'(0)$ of water-based MWCNT-nanofluid as a function stretching rate ratio parameter A when $Pr = 6.2$, $\beta = 0.2$, and $\varphi = 0.2$
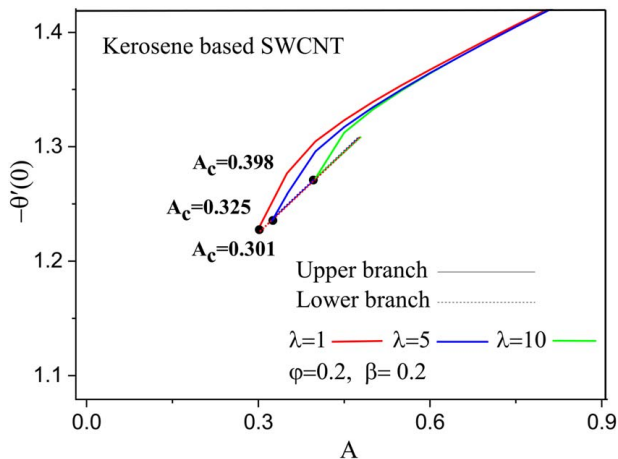

Fig. 8 Effects of λ on reduced heat transfer $-\theta'(0)$ of kerosene-based SWCNT as a function stretching sheet ratio parameter A when $Pr = 6.2$, $\beta = 0.2$, and $\varphi = 0.2$
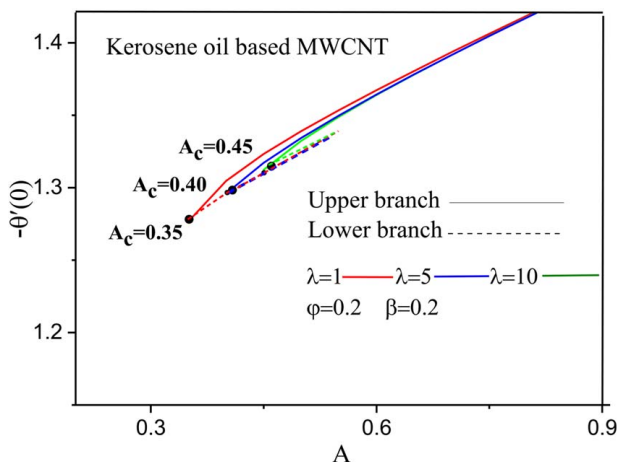

Fig. 9 Effects of λ on reduced heat transfer $-\theta'(0)$ of kerosene-based MWCNT as a function stretching sheet ratio parameter A when $Pr = 6.2$, $\beta = 0.2$, $\varphi = 0.2$

Table 6 Critical values A_c with representative values of β

β	Water SWCNT (A_c)	Water MWCNT (A_c)	Kerosene oil SWCNT (A_c)	Kerosene oil MWCNT (A_c)
0.1	−1.092	−1.129	−0.499	−0.832
0.2	−1.023	−1.051	−0.433	−0.807
0.3	−0.989	−1.011	−0.425	−0.799
0.5	−0.82	−0.831	−0.410	−0.781
1.0	−0.46	−0.492	−0.391	−0.750

associated depletion in heat transfer *to the wall*. In Fig. 9, for a value of reciprocal magnetic Prandtl number $\lambda = 1$, we obtain a critical value $A_c = 0.35$ and for a magnetic Prandtl number of $\lambda = 5$ the range of A_c values where solutions exist is contracted to ($A > A_c = 0.40$) for kerosene-oil-based MWCNT. A subsequent boost in reciprocal of magnetic Prandtl number to $\lambda = 10$ further reduces the critical range of stretching sheet ratio parameters to $A > A_c = 0.45$. Again, there is a suppression in reduced heat transfer with greater reciprocal of magnetic Prandtl number λ for kerosene-oil-based MWCNT-nanofluids. Evidently, SWCNT-nanofluid attains higher heat transfer rates than MWCNT-nanofluids, and this is probably attributable to the superior thermal conductivity of SWCNTs as compared to MWCNTs. It is also demonstrated that kerosene-oil-based CNTs have higher heat transfer than water-based CNTs. The different critical values of the stretching sheet ratio parameter, A_c with representative values of the magnetic parameter for water- and kerosene-oil-based CNTs are summarized in Table 6.

Table 7 displays the behavior of wall skin friction $\mathrm{Re}_x^{\frac{1}{2}} C_f$ and heat transfer rate $\mathrm{Re}_x^{-\frac{1}{2}} \mathrm{Nu}_x$ with increasing solid volume fraction parameter and magnetic parameter for both water-based SWCNT and MWCNT-nanofluids. Shear stress is clearly enhanced with an increase in solid volume fraction parameters for both SWCNT and MWCNT cases, i.e., greater doping of the nanofluid produces flow acceleration. On the other hand, a decay is observed in shear stress with an increasing magnetic parameter which is due to the retardation in the flow with a stronger magnetic field. Heat transfer rates are consistently elevated with solid volume fraction parameter and magnetic parameter for both CNT cases.

Table 8 presents values for wall shear stress and heat transfer rates with increasing solid volume fraction parameter and magnetic parameter for kerosene-based SWCNT and MWCNT-nanofluids. A boost in shear stress is induced with a higher solid volume fraction parameter for both SWCNT and MWCNT. On the other hand, a reduction in shear stress (i.e., retardation) is produced with increasing magnetic parameters. Heat transfer rate is again accentuated with solid volume fraction parameter and magnetic parameter for both CNT cases. Tables 7 and 8 imply that kerosene oil achieves higher shear stress and heat transfer rates than water as the base fluid.

5.5 Analysis of Velocity, Temperature, and Induced Magnetic Field Profiles. A detailed analysis has been performed for the effect of several selected parameters on the stagnation point flow regime. Both the flow and heat transfer analysis of single and multiple walls CNTs suspended in two different types of base fluids (water and kerosene-oil) have been investigated. The numerical solutions and the dual solutions are depicted graphically for velocity, temperature, and magnetic field profiles in Figs. 10–15. Both upper branch (first) and lower branch (second) solutions are shown. For brevity, only the magnetic parameter (β) effect is considered here since the other parameters have already been addressed in previous graphs. These profiles satisfy the boundary conditions and converge asymptotically. The dual solutions can be seen clearly from the figures. It is observed that the *first solution* has a thinner boundary-layer thickness as compared to the *second solution*. The first solution is considered stable while the second solution is considered unstable, and it has no physical significance.

Table 7 Numerical values of shear stress at wall and rate of heat flux of water-based SWCNT and MWCNT-nanofluids with solid volume fraction (φ) for different values of magnetic parameter (β) when Pr = 6.2, $A = 0.5$, $\lambda = 1$

		$Re_x^{\frac{1}{2}} C_f$			$Re_x^{\frac{-1}{2}} Nu_x$		
	φ	$\beta = 0$	$\beta = 0.1$	$\beta = 0.2$	$\beta = 0$	$\beta = 0.1$	$\beta = 0.2$
SWCNT	0	0.66726	0.577950	0.446003	1.8580	1.876670	1.903357
	0.1	0.85507	0.736923	0.565888	3.1057	3.159220	3.235171
	0.2	1.01387	0.869844	0.665413	3.7147	3.788875	3.894487
MWCNT	0	0.66726	0.577950	0.446003	1.8589	1.876670	1.903357
	0.1	0.81079	0.696282	0.533047	3.0351	3.084625	3.153542
	0.2	1.858860	0.797087	0.607711	3.5933	3.699611	3.792988

Table 8 Numerical values of shear stress at wall and rate of heat flux of kerosene-based SWCNT and MWCNT-nanofluids with solid volume fraction (φ) for different values of magnetic parameter (β) when Pr = 21, $A = 0.5$, $\lambda = 1$

		$Re_x^{\frac{1}{2}} C_f$			$Re_x^{\frac{-1}{2}} Nu_x$		
	φ	$\beta = 0$	$\beta = 0.1$	$\beta = 0.2$	$\beta = 0$	$\beta = 0.1$	$\beta = 0.2$
SWCNT	0	0.6672	0.577950	0.446003	3.5215	3.540253	3.5678
	0.1	0.8851	0.764710	0.588562	6.5623	6.632437	6.7375
	0.2	1.0671	0.918646	0.704716	8.0980	8.203925	8.3521
MWCNT	0	0.6672	0.577950	0.446003	3.5212	3.540253	3.5678
	0.1	0.8304	0.714288	0.547549	6.4462	6.502863	6.5986
	0.2	0.9696	0.829954	0.633318	7.9914	8.085865	8.2144

Effect of Magnetic Parameter (β) *on Water- and Kerosene-Based SWCNT.* The influence of magnetic parameter (β) on velocity, magnetic field, and temperature are depicted in Figs. 10–12, respectively, for water- and kerosene-oil-based SWCNT-nanofluids. In Fig. 10, the velocity profiles clearly show the existence of a dual solution when $A > A_c$ with variation in β. It is evident that the first solution is stable as the velocity profile enters the positive range and the second solution is unstable as the velocity profile enters the negative range. Here, the behavior of velocity near the walls and center deviates for each solution. Velocity is a minimum along the centerline and maximum at the walls. It is apparent that there is a substantial enhancement in velocity rises with an increase in magnetic parameter, $\beta \left(= \frac{\mu}{4\pi\rho_f} \frac{H_0^2}{c^2} \right)$ for the *first solution*. For the *second solution*, however, velocity decreases initially near the stretching sheet, and thereafter, the opposite trend is witnessed,

i.e., flow acceleration. Velocity for kerosene-oil-based SWCNT is lower for the first solution and higher for the second solution than that of water-based SWCNT.

The response in velocity is different compared with the influence of the magnetic body force parameter, $= \frac{\mu}{4\pi\rho_f} \frac{H_0^2}{c^2}$, which generally induces deceleration (as observed in the earlier skin friction plots).

In Fig. 11, a marked enhancement in the induced magnetic field is displayed for increasing magnetic parameter (β); furthermore, the existence of the dual solution is confirmed when $A > A_c$ with a variation in β. As we see, the *first solution is linearly stable* and physically realizable whereas the *second solution is clearly unstable*. For the first solution, kerosene-oil-based SWCNT-nanofluid attains greater magnetic induction magnitudes as compared to water-based SWCNT-nanofluid and the magnetic boundary-layer thickness increases. The second solution also exhibits a noticeable increase in magnitudes but has no immediate practical significance in
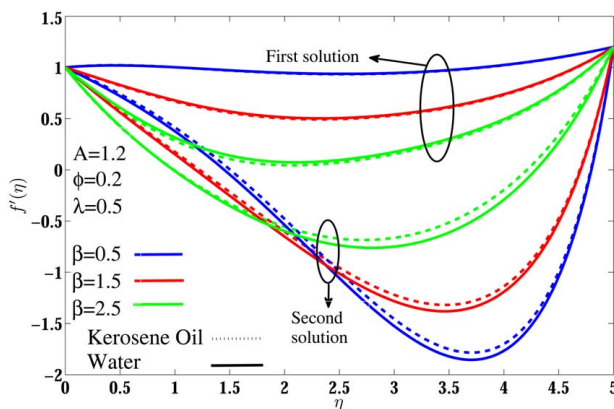

Fig. 10 Effects of β on velocity profiles (f') for water- and kerosene-oil-based SWCNT when Pr = 6.2 (water), and Pr = 21 (kerosene –oil)
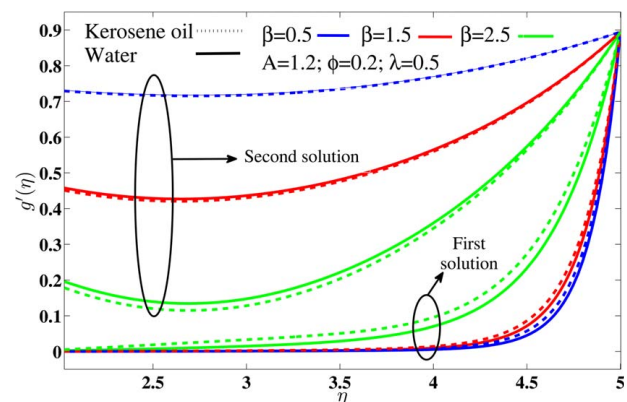

Fig. 11 Effects of β on magnetic induction profiles for water- and kerosene-oil-based SWCNT when $Pr = 6.2$ (Water), $Pr = 21$ (kerosene-oil)
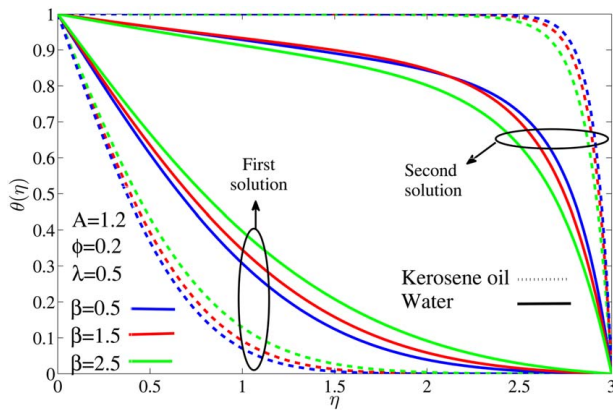
Fig. 12 Effects of β on temperature profiles (θ) for water and kerosene-oil-based SWCNT when $Pr = 6.2$ (Water), $Pr = 21$ (kerosene-oil)
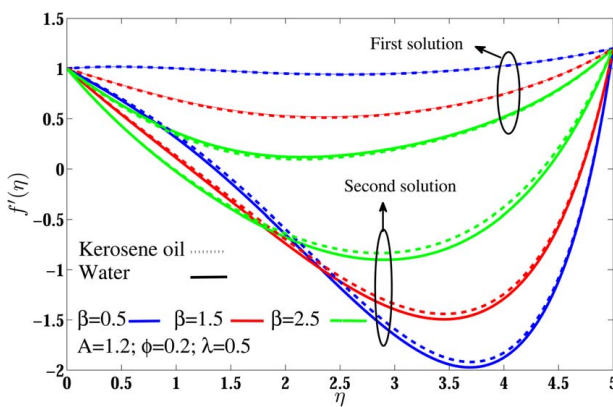

Fig. 13 Effects of β on velocity distribution for water and kerosene-oil-based MWCNT when Pr = 6.2 (water), Pr = 21 (kerosene oil)
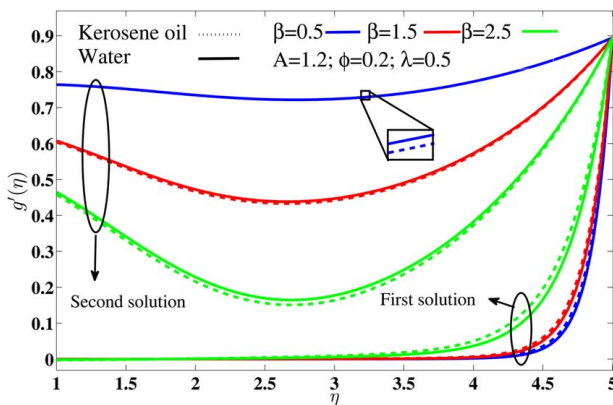

Fig. 14 Effects of β on induced magnetic field function for water- and kerosene-oil-based MWCNT when Pr = 6.2 (water) and Pr = 21 (kerosene oil)

nanomaterials processing flows, due to the negative values within the boundary layer. Figure 12 shows that temperature is also dramatically modified with an increase in magnetic parameter (β); it is clearly an *increasing function* of rising magnetic parameter (β), and the dual solution is observed when $A > A_c$. Evidently, the thermal energy is generated in the CNT nanofluid with the greater magnetic field, since supplementary work is expended in dragging

the nanofluid against the action of the magnetic field, as noted by other researchers including Kumari et al. [44] and Ghosh et al. [46]. The first solution is stable, and the second solution is again unstable. An increase in temperature is observed for the first solution and a decrease is observed for the second solution in the case of kerosene CNT nanofluid case; however, both solutions exhibit an increase in magnitude for the water CNT nanofluid with an increase in magnetic parameter. For the first solution, the temperature is lower for kerosene-oil-based SWCNT and higher for water-based SWCNT-nanofluid. The contrary response is computed for the second solution which again has no physical significance in materials engineering applications, due to the negative values within the boundary layer. The thermal boundary-layer thickness is consistently enhanced for the first solution with water CNT nanofluid.

Effect of Magnetic Parameter (β) on Water/Kerosene-Based MWCNT Nanofluids. The influence of magnetic parameter (β) on velocity, induced magnetic field, and temperature are depicted in Figs. 13–15, respectively, for water- and kerosene-oil-based MWCNT. Figure 13 exhibits a dual solution when $A > A_c$ with different values of β. The first solution is stable as the velocity profile occurs in the positive range and the second solution is unstable as the velocity profile is in the negative range. Dissimilar behavior is computed near the walls and in the central zone, for both solutions. Velocity is again boosted with an increase in magnetic parameters for the first solution. For the second solution, there is an *initial deceleration* sustained near the stretching sheet (wall) with a subsequent reversal in this trend.

Velocity for kerosene-oil-based MWCNT is lower than that of water-based MWCNT for the first solution and higher for the second solution. At the boundaries, velocity is zero for both base fluids. However, the second solutions have no physical significance as explained earlier. SWCNTs achieve higher velocities than MWCNT-nanofluids. SWCNTs possess greater densities as compared to MWCNTs and a greater thermal conductivity as shown earlier in Table 1, which leads to enhancement of heat absorption; this in turn encourages momentum diffusion, i.e., energizes the nanofluid flow so that SWCNTs achieve higher velocity than MWCNTs. In Fig. 14, an enhancement in the induced magnetic field is found with increasing magnetic parameter (β) and a dual solution when $A > A_c$. Again, the first solution is linearly stable and is physically realizable and the second solution is unstable. For the first solution, kerosene-oil-based SWCNT achieves higher magnetic induction field values as compared to water-based SWCNT-nanofluid, and the magnetic boundary-layer thickness is greater also. A similar response is observed for the second solution. It is also noteworthy that although magnetic field can induce a current in the conductive nanofluid, the dominant effect of the magnetic parameter is to mobilize the Lorentzian resistive force.

Figure 15 reveals that temperature is a decreasing function of rising magnetic parameter (β) and shows the existence of the dual solution when $A > A_c$. The first solution is stable, and the second solution is unstable. An increase in temperature is observed for the first solution, and a decrease is observed for the second solution with an increase in magnetic parameters. For the first solution, temperature magnitudes are lower for kerosene-oil-based SWCNT and greater for water-based SWCNT; the reverse trend is observed for the second solution. The thermal boundary-layer thickness decreases for the first solution for both water- and kerosene-based CNT nanofluids. In the case of the second solution, however, thermal boundary-layer thickness increases for both base fluids. Overall, higher temperatures are computed for SWCNTs as compared to MWCNTs.

5.6 Comparison of SWCNT With MWCNT for the Effects of Significant Parameters. Figures 16–18 illustrate the behavior of velocity profile, induced magnetic field profile, and temperature profile, respectively, for significant values of the
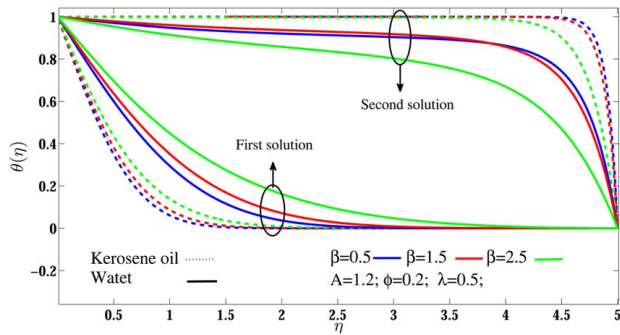
Fig. 15 Effects of β on temperature profile for water- and kerosene-oil-based MWCNT when $Pr = 6.2$ (water) and $Pr = 21$ (kerosene oil)
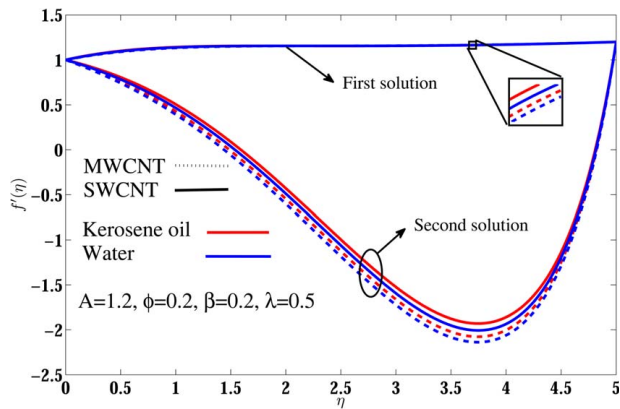

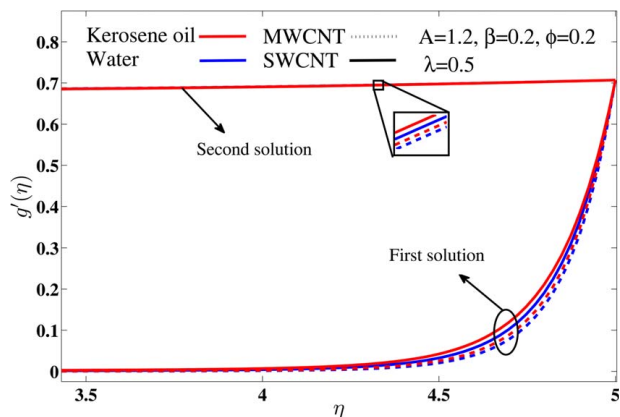**Fig. 16 Velocity profile of water- and kerosene-oil-based SWCNT and MWCNT for certain values of Pr, φ, β, λ**

Fig. 17 Induced magnetic field profile of water- and kerosene-oil-based SWCNT and MWCNT for certain values of Pr, φ, β, λ

dimensionless parameters for both water- and kerosene-oil-based SWCNT and MWCNT. It is observed that kerosene oil provides higher velocity than water, and however, SWCNT provides higher velocity as compared to MWCNT, concluding kerosene-based SWCNT has a higher velocity than others. This is due to the greater density and greater thermal conductivity of SWCNT as compared to MWCNT as shown in Table 5.1, which leads to enhancement of heat absorption; hence, their velocity is greater than MWCNT. The magnetic field profile also shows the same pattern. But opposite phenomena are revealed for temperature profile.
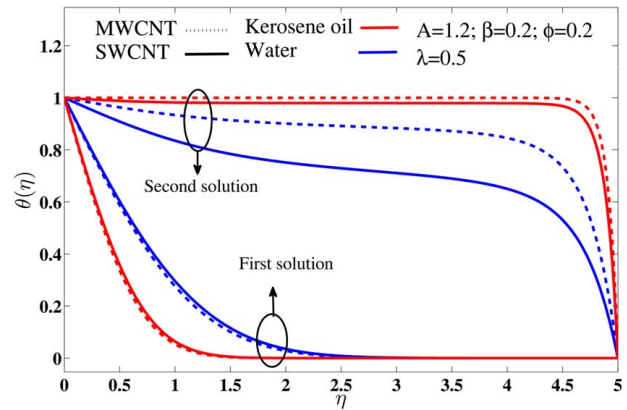

Fig. 18 Temperature profile of water- and kerosene-oil-based SWCNT and MWCNT for certain values of Pr, φ, β, λ

6 Conclusions

A theoretical model has been developed for magnetohydrodynamic stagnation (Hiemenz) boundary-layer flow and forced convection heat transfer in an incompressible viscous nanofluid containing carbon nanotubes (CNTs) from a linearly stretching sheet. Magnetic induction effects have been incorporated. Similarity solutions have been derived where possible in addition to dual branch solutions. Both single-wall carbon nanotubes (SWCNTs) and multi-wall carbon nanotubes (MWCNTs) have been studied in addition to water and kerosene oil as base fluids. With Lie-group transformations, the partial differential continuity, momentum, magnetic induction, and heat conservation equations have been rendered into a system of nonlinear ordinary differential equations. Numerical solutions to the ordinary differential boundary value problem have been obtained with the bvp4c solver in MATLAB. Validation with earlier studies has been included. Computations of reduced skin friction and reduced wall heat transfer rate (Nusselt number) are also included in order to identify the critical parameter values for the existence of dual solutions (upper and lower branch solutions are separated by a critical point) for velocity, temperature, and induced magnetic field functions. Dual solutions are shown to exist for some cases studied. The following conclusions can be drawn from the present analysis.

(1) Skin friction decreases with an increase in the carbon nanotube (CNT) volume fraction parameter whereas the heat transfer rate increases.

(2) Skin friction and Nusselt number are both increasing functions of the sheet stretching rate ratio parameter.

(3) SWCNTs possess greater densities (as compared to MWCNTs) and a greater thermal conductivity, which results in larger modifications in skin friction and Nusselt number.

(4) Kerosene-oil-based CNT nanofluids produce greater skin friction and heat transfer rates as compared to water-based CNT nanofluids.

(5) For rising values of the magnetic parameter, both velocity and induced magnetic field are enhanced when stretching rate ratio parameter is less than 1.

(6) Fluid velocity is generally elevated with a rise in reciprocal of magnetic Prandtl number, i.e., with greater magnetic diffusivity of the nanofluid.

(7) Overall SWCNTs achieve superior heat transfer performance as compared to MWCNTs.

(8) In the dual solutions, the first (*upper branch*) solution is stable and feasible whereas the second (*lower branch*) solution is unstable and not practical.

(9) For the first solution, kerosene-oil-based SWCNT achieves higher magnetic induction field values (and magnetic boundary-layer thickness) as compared to water-based SWCNT-nanofluid.

The present study has revealed some interesting features of electroconductive CNT nanofluid dynamics from a stretching sheet. Although magnetic induction effects have been included, *Maxwell displacement* currents [46] and *unsteady* effects [66] have been ignored. These may be considered in the future and provide further refinement in magnetofluid dynamic models of CNT nanofluids for enhancing thermal conductivity in kerosene-oil- and water base fluids.

Conflict of Interest

There are no conflicts of interest. This article does not include research in which human participants were involved. Informed consent is not applicable. This article does not include any research in which animal participants were involved.

Data Availability Statement

No data, models were generated or used for this paper.

Nomenclature

A = stretching rate ratio parameter
T = fluid temperature inside the boundary layer
c_p = specific heat at constant pressure
q_w = wall heat flux
C_f = local skin friction coefficient
H_0 = upstream magnetic field at infinity
T_∞ = freestream fluid temperature
T_0 = ambient temperature
T_w = surface temperature
$\bar{H}_e$ = freestream magnetic field
$\bar{U}_e$ = freestream velocity
$\bar{U}_w$ = velocity of stretching sheet
$(c_p)_{nf}$ = specific heat of nanofluid
$(c_p)_{CNT}$ = specific heat of carbon nanotube
$f'(\eta)$ = dimensionless velocity
$g'(\eta)$ = dimensionless induced magnetic field
$(\bar{H}_1, \bar{H}_2)$ = induced magnetic field components along the x and y-directions, respectively
Nu_x = local Nusselt number
Pr = Prandtl number
Re_x = local Reynolds number
$(\bar{u}, \bar{v})$ = velocity components along the x and y-directions, respectively
$(\bar{x}, \bar{y})$ = Cartesian coordinate system

Greek Symbols

α_{nf} = thermal diffusivity of nanofluid
β = magnetic parameter
$\theta(\eta)$ = dimensionless temperature
κ = thermal conductivity of the fluid
κ_{nf} = thermal conductivity of the nanofluid
κ_{CNT} = thermal conductivity of carbon nanotube
κ_∞ = thermal conductivity of the fluid in the freestream
λ = reciprocal magnetic Prandtl number
μ = dynamic viscosity of the fluid
μ_{nf} = dynamic viscosity of the nanofluid
μ_∞ = dynamic viscosity of the fluid in the freestream
ν = kinematic viscosity
ν_{nf} = kinematic viscosity of the nanofluid
ν_∞ = kinematic viscosity in the freestream
ρ_∞ = freestream fluid density
ρ_{nf} = density of the nanofluid
ρ_{CNT} = density of carbon nanotube
τ_w = wall shear stress
φ = solid volume fraction parameter
φ_w = nanoparticle volume fraction at the surface
φ_∞ = ambient values of nanoparticle volume fraction

References

[1] Batteh, J. J., Chen, M. M., and Mazumder J., 2000, "A Stagnation Flow Analysis of the Heat Transfer and Fluid Flow Phenomena in Laser Drilling," ASME J. Heat Transfer-Trans. ASME, **122**(4), pp. 801–807.

[2] Hasegawa, M., and Sakaue, H., 2018, "Microfiber Coating for Drag Reduction by Flocking Technology," Coatings, **8**(12), p. 464.

[3] Memon, N., and Jaluria, Y., 2011, "Flow Structure and Heat Transfer in a Stagnation Flow CVD Reactor," ASME J. Heat Transfer-Trans. ASME, **133**(8), p. 082501.

[4] Wang, C. Y., 2008, "Stagnation Flow Towards a Shrinking Sheet," Int. J. Non linear Mech., **43**(5), pp. 377–382.

[5] Mehmood, R., Rana, S., Anwar Bég, O., and Kadir, A., 2018, "Numerical Study of Chemical Reaction Effects in Magnetohydrodynamic Oldroyd-B Oblique Stagnation Flow With a Non-Fourier Heat Flux Model," J. Braz. Soc. Mech Sci. Eng., **40**(11), p. 526.

[6] Jaluria, Y., 2018, "Continuous Materials Processing," *Advanced Materials Processing and Manufacturing. Mechanical Engineering Series*. Springer, Cham.

[7] Scheid, B., Quiligotti, S., Tran, B., and Stone, H. A., 2009, "Lateral Shaping and Stability of a Stretching Viscous Sheet," Eur. Phys. J. B, **68**(4), pp. 487–494.

[8] Uddin, M. J., Anwar Bég, O., and Uddin, M. N., 2016, "Energy Conversion Under Conjugate Conduction, Magneto-Convection, Diffusion and Nonlinear Radiation Over a Non-linearly Stretching Sheet With Slip and Multiple Convective Boundary Conditions," Energy, **115**, pp. 1119–1129.

[9] Sakiadis, B. C., 1961, "Boundary-Layer Behavior on Continuous Solid Surfaces: I. Boundary-Layer Equations for Two-Dimensional and Axisymmetric Flow," AIChE J, **7**(1), pp. 26–28.

[10] Crane, L. J., 1970, "Flow Past a Stretching Plate," Z. Angew. math. phys., **21**(4), pp. 645–647.

[11] Dandapat, B. S., Santra, B., and Vajravelu, K., 2007, "The Effects of Variable Fluid Properties and Thermocapillarity on the Flow of a Thin Film on an Unsteady Stretching Sheet," Int. J. Heat Mass Transfer, **50**(5–6), pp. 991–996.

[12] Tsai, R., Huang, K. H., and Huang, J. S., 2008, "Flow and Heat Transfer Over an Unsteady Stretching Surface With a Non-uniform Heat Source," Int. Commun. Heat Mass Transfer, **35**(10), pp. 1340–1343.

[13] Bhattacharyya, K., Mukhopadhyay, S., and Layek, G. C., 2011, "Slip Effects on an Unsteady Boundary Layer Stagnation-Point Flow and Heat Transfer Towards a Stretching Sheet," Chin. Phys. Lett., **28**(9), p. 094702.

[14] Chen, W., Zou, C., and Li, X., 2019, "Application of Large-Scale Prepared MWCNTs Nanofluids in Solar Energy System as Volumetric Solar Absorber," Sol. Energy Mater. Sol. Cells, **200**, p. 109931.

[15] Sivaraj, R., and Banerjee, S., 2021, "Transport Properties of Non-Newtonian Nanofluids and Applications," Eur. Phys. J. Spec. Top. , **230**, pp. 1167–1171.

[16] Prakash, J., Tripathi, D., and Bég, O.A. , 2020, "Comparative Study of Hybrid Nanofluids in Microchannel Slip Flow Induced by Electroosmosis and Peristalsis," Appl. Nanosci., **10**, pp. 1693–1706.

[17] Yang, L., Huang, J.-N., Ji, W., and Mao, M., 2020, "Investigations of a New Combined Application of Nanofluids in Heat Recovery and Air Purification," Powder Technol., **360**, pp. 956–966.

[18] Choi, S. U. S., Zhang, Z. G., Yu, W., Lockwood, F. E., and Grulke, E. A., 2001, "Anomalous Thermal Conductivity Enhancement in Nanotube Suspensions," Appl. Phys. Lett., **79**(14), pp. 2252–2254.

[19] Masuda, H., Ebata, A., Teramae, K., and Hishinuma, N., 1993, "Alteration of Thermal Conductivity and Viscosity of Liquid by Dispersing Ultra-fine Particles," Netsu Bussei, **4**(4), pp. 227–233.

[20] Das, S. K., Putra, N., Thiesen, P., and Roetzel, W., 2003, "Temperature Dependence of Thermal Conductivity Enhancement for Nanofluids," ASME J. Heat Transfer-Trans. ASME, **125**(4), pp. 567–574.

[21] Xuan, Y., and Li, Q., 2003, "Investigation on Convective Heat Transfer and Flow Features of Nanofluids," ASME J. Heat Transfer-Trans. ASME, **125**(1), pp. 151–155.

[22] Pak, B. C., and Cho, Y. I., 1998, "Hydrodynamic and Heat Transfer Study of Dispersed Fluids With Submicron Metallic Oxide Particles," Exp. Heat Transfer, **11**(2), pp. 151–170.

[23] Trisaksri, V., and Wongwises, S., 2007, "Critical Review of Heat Transfer Characteristics of Nanofluids," Renewable Sustainable Energy Rev., **11**(3), pp. 512–523.

[24] Wang, X.-Q., and Mujumdar, A. S., 2007, "Heat Transfer Characteristics of Nanofluids: A Review," Int. J. Therm. Sci., **46**(1), pp. 1–19.

[25] Eastman, J. A., Choi, S. U. S., Li, S., Yu, W., and Thompson, L. J., 2001, "Anomalously Increased Effective Thermal Conductivities of Ethylene Glycol-Based Nanofluids Containing Copper Nanoparticles," Appl. Phys. Lett., **78**(6), pp. 718–720.

[26] Mehmood, R., Tabassum, R., Kuharat, S., Anwar Bég, O., and Babaie, M., 2018, "Thermal Slip in Oblique Radiative Nano-Polymer Gel Transport With Temperature-Dependent Viscosity: Solar Collector Nanomaterial Coating Manufacturing Simulation," Arabian J. Sci. Eng., **44**(2), pp. 1525–1541.

[27] Ding, Y., Alias, H., Wen, D., and Williams, R. A., 2006, "Heat Transfer of Aqueous Suspensions of Carbon Nanotubes (CNT Nanofluids)," Int. J. Heat Mass Transfer, **49**(1–2), pp. 240–250.

[28] De Volder, M. F. L., Tawfick, S. H., Baughman, R. H., and Hart, A. J., 2013, "Carbon Nanotubes: Present and Future Commercial Applications," Science, **339**(6119), pp. 535–539.

[29] Akbar, N. S., Khan, Z. H., and Nadeem, S., 2014, "The Combined Effects of Slip and Convective Boundary Conditions on Stagnation Point Flow of CNT Suspended Nanofluid Over a Stretching Sheet," J. Mol. Liq., **196**, pp. 21–25.

[30] Akbar, N. S., Shoaib, M., Tripathi, D., Bhushan, S., and Anwar Bég, O., 2018, "Analytical Approach for Entropy Generation and Heat Transfer Analysis of CNT-Nanofluids Through Ciliated Porous Medium," J. Hydrodyn. B, **30**(2), pp. 1–11.

[31] Ferraro, V. C. A., and Plumpton, C., 1961, *An Introduction to Magneto-Fluid Mechanics*, Oxford University Press, New York.

[32] Anwar Bég, O., Khan, M. S., Karim, I., Alam, M. M., and Ferdows, M., 2014, "Explicit Numerical Study of Unsteady Hydromagnetic Mixed Convective Nanofluid Flow From an Exponentially Stretching Sheet in Porous Media," Appl. Nanosci., **4**(8), pp. 943–957.

[33] Seth, G. S., and Mandal, P. K., 2019, "Analysis of Electromagnetohydrodynamic Stagnation Point Flow of Nanofluid Over a Nonlinear Stretching Sheet With Variable Thickness," J. Mech., **35**(5), pp. 719–733.

[34] Thumma, T., Anwar Bég, O., and Kadir, A., 2017, "Numerical Study of Heat Source/Sink Effects on Dissipative Magnetic Nanofluid Flow From a Non-Linear Inclined Stretching/Shrinking Sheet," J. Mol. Liq., **232**, pp. 159–173.

[35] Yavari, M., Mansourpour, Z., and Shariaty-Niassar, M., 2019, "Controlled Assembly and Alignment of CNTs in Ferrofluid: Application in Tunable Heat Transfer," J. Magn. Magn. Mater., **4791**, pp. 170–178.

[36] Masotti, A., and Caporali, A., 2013, "Preparation of Magnetic Carbon Nanotubes (MAG-CNTS) for Biomedical and Biotechnological Applications," Int. J. Mol. Sci., **14**(12), pp. 24619–24642.

[37] Rossella, F., Soldano, C., Bellani, V., and Tommasini, M., 2012, "Metal-Filled Carbon Nanotubes as a Novel Class of Photothermal Nanomaterials," Adv. Mater., **24**(18), pp. 2453–2458.

[38] Korneva, G., Ye, H., Gogotsi, Y., Halverson, D., Friedman, G., Bradley, J. C., and Kornev, K. G., 2005, "Carbon Nanotubes Loaded With Magnetic Particles," Nano Lett., **5**(5), pp. 879–884.

[39] Pal, S., Chandra, S., Phan, M. H., Mukherjee, P., and Srikanth, H., 2009, "Carbon Nanostraws: Nanotubes Filled With Superparamagnetic Nanoparticles," Nanotechnology, **20**(48), p. 485604.

[40] Shi, L., He, Y., Hu, Y., and Wang, X., 2018, "Thermophysical Properties of Fe_3O_4@CNT Nanofluid and Controllable Heat Transfer Performance Under Magnetic Field," Energy Convers. Manage., **177**, pp. 249–257.

[41] Sidik, N. A. C., Yazid, M. N. A. W. M., and Samion, S., 2017, "A Review on the Use of Carbon Nanotubes Nanofluid for Energy Harvesting System," Int. J. Heat Mass Transfer, **111**, pp. 782–794.

[42] Hong, H., Wright, B., Wensel, J., Jin, S., Ye, X. R., and Roy, W., 2007, "Enhanced Thermal Conductivity by the Magnetic Field in Heat Transfer Nanofluids Containing Carbon Nanotubes," Synth. Met., **157**(10–12), pp. 437–440.

[43] Liu, W. I., Alsarraf, J., Shahsavar, A., Rostamzadeh, M., Afrand, M., and Nguyen, T. K., 2019, "Impact of Oscillating Magnetic Field on the Thermal-Conductivity of Water-Fe3O4 and Water-Fe3O4/CNT Ferro-Fluids: Experimental Study," J. Magn. Magn. Mater., **48415**, pp. 258–265.

[44] Kumari, M., Takhar, H. S., and Nath, G., 1990, "MHD Flow and Heat Transfer Over a Stretching Surface With Prescribed Wall Temperature or Heat Flux," Heat Mass Transfer, **25**, pp. 331–336.

[45] Koshiba, Y., Matsushita, T., and Ishikawa, M., 2002, "Influence of Induced Magnetic Field on Large Scale Pulsed MHD Generator," Proceedings of the AIAA 33rd Plasma Dynamics and Lasers Conference, Maui, HI, May 20–23, pp. 3002–2145.

[46] Ghosh, S. K., Anwar Bég, O., Zueco, J., and Prasad, V. R., 2010, "Transient Hydromagnetic Flow in a Rotating Channel Permeated by an Inclined Magnetic Field With Magnetic Induction and Maxwell Displacement Current Effects," Z. Angew. Math. Phys., **61**, pp. 147–169.

[47] Anwar Bég, O., Ferdows, M., Islam, S., and Islam, M. N., 2014, "Numerical Simulation of Marangoni Magnetohydrodynamic Bio-Nanofluid Convection From a Non-Isothermal Surface With Magnetic Induction Effects: A Bio-Nanomaterial Manufacturing Transport Model," J. Mech. Med. Biol., **14**(3), p. 1450039.

[48] Anwar Bég, O., Kuharat, S., Ferdows, M., Das, M., Kadir, A., and Shamshuddin, M., 2019, "Magnetic Nano-Polymer Flow with Magnetic Induction and Nanoparticle Solid Volume Fraction Effects: Solar Magnetic Nano-Polymer Fabrication Simulation," Proc. Inst. Mech. Eng., Part N: J Nanoeng. Nanomater. Nanosyst., **233**(1), pp. 27–45.

[49] Uddin, M. J., Kabir, M. N., Anwar Bég, O., and Alginahi, Y., 2018, "Chebyshev Collocation Computation of Magneto-Bioconvection Nanofluid Flow Over a Wedge With Multiple Slips and Magnetic Induction," Proc. Inst. Mech. Eng., Part N: J Nanoeng. Nanomater. Nanosyst., **232**(4), pp. 109–122.

[50] Iqbal, Z., Azhar, E., and Maraj, E. N., 2017, "Transport Phenomena of Carbon Nanotube and Bioconvection Nanoparticles on Stagnation Point Flow in Presence of Induced Magnetic Field," Phys. E, **91**, pp. 128–135.

[51] Gireesha, B. J., Mahanthesh, B., Shivakumara, I. S., and Eshwarappa, K. M., 2016, "Melting Heat Transfer in Boundary Layer Stagnation Point Flow of Nanofluid Toward a Stretching Sheet With Induced Magnetic Field," Eng. Sci. Technol. Int. J, **19**, pp. 313–321.

[52] Maxwell, J. C., 1904, *A Treatise on Electricity and Magnetism*, 3rd ed., Oxford, UK.

[53] Jeffrey, D. J., 1973, "Conduction Through a Random Suspension of Spheres," Proc. R. Soc. A, **335**, pp. 355–367.

[54] Davis, R., 1986, "The Effective Thermal Conductivity of a Composite Material With Spherical Inclusions," Int. J. Thermophys., **7**(3), pp. 609–620.

[55] Hamilton, R. L., and Crosser, O. K., 1962, "Thermal Conductivity of Heterogeneous Two Component Systems," Ind. Eng. Chem. Fundam., **1**(3), pp. 182–191.

[56] Xue, Q. Z., 2005, "Model for Thermal Conductivity of Carbon Nanotube-Based Composites," Phys. B, **368**(1–4), pp. 302–307.

[57] Hamad, M. A. A., 2011, "Analytical Solution of Natural Convection Flow of a Nanofluid Over Linearly Stretching Sheet in the Presence of Magnetic Field," Int. Commun. Heat Mass Transfer, **38**(4), pp. 487–492.

[58] Ibrahim, F. S., Mansour, M. A., and Hamad, M. A. A., 2005, "Lie-Group Analysis of Radiation and Magnetic Field Effects on Free Convection and Mass Transfer Flow Past a Semiinfinite Vertical Flat Plate," Electron. J. Differ. Equ., **2005**, pp. 1–17.

[59] Mukhopadhyay, S., Layek, G. C., and Samad, S. A., 2005, "Study of MHD Boundary Layer Flow Over a Heated Stretching Sheet with Variable Viscosity," Int. J. Heat Mass Transfer, **48**(21–22), pp. 4460–4466.

[60] Kandasamy, R., and Muhaimin, I., 2010, "Scaling Transformation for the Effect of Temperature-Dependent Fluid Viscosity With Thermophoresis Particle Deposition on MHD-Free Convection Heat and Mass Transfer Over a Porous Stretching Surface," Transp. Porous Media, **84**(2), pp. 549–565.

[61] Muhaimin, I., Kandasamy, R., and Hashim, I., 2010, "Scaling Transformation for the Effect of Chemical Reaction on Free Convection Heat and Mass Transfer in the Presence of Variable Stream Conditions," Chem. Eng. Res. Des., **88**(10), pp. 1320–1328.

[62] Hamad, M. A. A., and Pop, I., 2011, "Scaling Transformations for Boundary Layer Stagnation-Point Flow Towards a Heated Permeable Stretching Sheet in a Porous Medium Saturated with a Nanofluid and Heat Absorption/Generation Effects," Transp. Porus Media, **87**(1), pp. 25–39.

[63] Ali, F. M., Nazar, R., Arifin, N. M., and Pop, I., 2011, "MHD Stagnation-Point Flow and Heat Transfer Towards Stretching Sheet with Induced Magnetic Field," Appl. Math. Mech., **32**(4), pp. 409–418.

[64] Hayat, T., Farooq, M., and Alsaedi, A., 2015, "Homogenous-Heterogeneous Reactions in the Stagnation Point Flow of Carbon Nanotubes with Newtonian Heating," AIP Adv., **5**, p. 027130.

[65] Hayat, T., Muhammad, K., Farooq, M., and Alsaedi, A., 2016, "Melting Heat Transfer in Stagnation Point Flow of CNTs Towards Variable Thickness Surface," AIP Adv., **6**(1), pp. 015214–015216.

[66] Vasu, B., Ray, A. K., Anwar Bég, O., and Gorla, R. S. R., 2019, "Magneto-Bioconvection Flow of a Casson Thin Film With Nanoparticles Over an Unsteady Stretching Sheet: HAM and GDQ Computation," Int. J. Numer. Methods Heat Fluid Flow, **29**(2), p. 33.